JOURNAL OF CATALYSIS **170,** 62–74 (1997)
ARTICLE NO. CA971738

Microstructural Evolution of γ-Alumina-Supported Rh upon Aging in Air

Zara Weng-Sieh,*,† Ronald Gronsky,*,† and Alexis T. Bell‡,§

*Materials Science and Mineral Engineering Department and ‡Chemical Engineering Department, University of California Berkeley; and †Materials Science Division and §Chemical Sciences Division, Lawrence Berkeley National Laboratory

Received February 21, 1996; revised April 22, 1997; accepted April 28, 1997

Microstructural changes in alumina-supported rhodium catalysts during aging in air at high temperatures were investigated using a combination of high-resolution transmission electron microscopy, X-ray photoelectron spectroscopy (XPS), and X-ray diffraction. Both constituents, particles and support, undergo structural changes during thermal aging. With increasing aging temperature and time, the support transforms from γ- to α-alumina, and the phase change is accelerated by the presence of rhodium. The rhodium, present initially as 10-Å-diameter metal particles, undergoes oxidation with the formation of a variety of oxide phases, depending on the temperature at which aging has occurred. At 500°C, highly dispersed, raft-like structures are observed. Continued aging at this temperature results in a coarsening of these structures to form three-dimensional particles of high-temperature, high-pressure (HT, HP) orthorhombic Rh_2O_3. At 850°C, aging causes severe coalescence of the HT, HP orthorhombic Rh_2O_3 particles, while at 1000°C, RhO_2 particles are observed together with large particles of HT, HP orthorhombic Rh_2O_3. A high Rh binding energy (near 309 eV) is observed using XPS following all aging treatments and may be attributed to either the HT, HP orthorhombic phase or to Rh^{4+}.

INTRODUCTION

Rhodium supported on γ-alumina is used in automotive catalytic converters to promote the reduction of NO (1, 2). Over the lifetime of the converter, microstructural changes in the rhodium and the support contribute to a loss in catalytic activity. Because of increasingly stringent federal and state regulations on the lifetime performance of the catalytic converter (3), there is a need to understand the fundamental processes that occur during the thermal aging of γ-alumina-supported rhodium.

Previously reported studies suggest that the microstructural changes that occur in γ-alumina-supported rhodium are different when thermal aging occurs below and above approximately 650°C. It has been inferred from indirect evidence that aging in air below 650°C results in the formation of highly dispersed rhodium oxide moieties (4–7). While near-edge extended absorption fine structure (NEXAFS) studies indicate that these oxide structures are orthorhombic Rh_2O_3 (8), X-ray photoelectron spectroscopy (XPS) spectra of the aged catalyst exhibit Rh(3*d*) peaks with binding energies significantly larger than that characteristic of Rh^{3+}. Reduction of air-aged catalysts results in the near complete reduction of the dispersed rhodium oxide back to metallic rhodium particles (4–7). Thermal aging in air at temperatures above 650°C results in the formation of particles of Rh_2O_3 (7, 9). The presence of RhO (8–11) and RhO_2 (12, 13) have also been suggested, as has the possibility that some of the rhodium diffuses into the support and thereby forms a rhodium spinel (4, 5). While bulk Rh_2O_3 is readily reducible between 200 and 400°C (14), the rhodium oxide phase formed during high-temperature aging is difficult to reduce at temperatures below 500–600°C (4, 5, 7–9). Sintering of the alumina support has also been observed, and it has been suggested that this process can lead to the occlusion of rhodium, making it inaccessible for catalysis (15).

The purpose of this study is to identify the dominant processes affecting the microstructural evolution of γ-alumina-supported rhodium catalysts upon aging in air. The time–temperature behavior of 1.5 wt% rhodium supported on high-surface-area γ-alumina has been characterized after aging in air at temperatures of 500, 850, and 1000°C for durations up to 102 h, using transmission electron microscopy (TEM), X-ray photoelectron spectroscopy (XPS), and X-ray diffraction (XRD). The microstructure of individual phases is identified from high-resolution transmission electron microscopy and X-ray diffraction techniques. The surface composition of Rh phases is discussed in terms of the chemical shifts measured by X-ray photoelectron spectroscopy.

METHODS

γ-Alumina-supported rhodium was prepared by incipient wetness impregnation of dried alumina (Degussa Alon C, 100 m^2/g) with an aqueous solution of rhodium(III) trichlorohydrate ($RhCl_3$–$3H_2O$) (Johnson–Matthey). The catalyst was then dried at 120°C for 2 h, calcined in air flowing at 100 cm^3/min at 400°C for 4 h, and reduced in H_2

0021-9517/97 $25.00

at 400°C for 4 h. The reduced catalyst was then passivated by exposure to 1000 ppm O_2/He at room temperature for 20 min. Samples of the catalyst were aged in air for 9, 56, and 102 h at 500°C; for 4, 25, and 56 h at 850°C; and for 5 h at 1000°C.

TEM specimens were prepared by crushing the catalyst between two glass slides and dry-dispersing the catalyst onto a holey-carbon covered TEM grid. HRTEM was performed on a Topcon 002B electron microscope operating at 200 kV, with a nominal point-to-point resolution of 1.9 Å. Image analysis was performed using GATAN's Digital Micrograph software. The method used for rhodium particle size measurement is described in an earlier report (16). Rhodium oxide phases were identified by Fourier analysis of HRTEM images, which provide precise measurements of their lattice spacings and interplanar angles. Because each rhodium oxide phase exhibits characteristic lattice spacings and interplanar angles that are unique to each phase, this procedure enables their identification.

A Siemens D5000 diffractometer equipped with a Cu $K\alpha$ source, operated at 30 kV and 40 mA, was used to obtain X-ray diffraction patterns. For identification of the phases of alumina, X-ray diffraction scans were acquired over angles between 26° and 70° at 0.1°/count and a rate of 2 sec/count. These angles include all of the major (significant) peaks for the γ-, δ-, θ-, and α-alumina phases reported in the JCPDF files. Since the γ-, δ-, and θ-alumina structures are closely related, many of their prominent X-ray diffraction peaks overlap significantly. Therefore, for clarity, small-angle scans were obtained at 0.02°–0.04°/count at a rate of 3–5 sec/count.

X-ray photoelectron spectroscopy was performed on a Perkin–Elmer PHI ESCA 5300 equipped with a Mg $K\alpha$ source (1253.5 eV). Supported catalysts were prepared for analysis by adhering the powders to one side of double-sided tape. Rh(3*d*) binding energies were determined using the Al(2*p*) binding energy at 73.9 eV as a reference (17). To relate the observed XPS features to rhodium oxidation states in a specific environment, X-ray photoelectron spectra of rhodium oxide standards were taken. As shown in Table 1, the Rh(3*d*) binding energies measured were 308.1 eV for hexagonal (LT, LP) Rh_2O_3, 308.3 eV for orthorhombic (HT, LP) Rh_2O_3, and 309.4 eV for tetragonal RhO_2. As indicated in Table 1, the first value is close to those reported in the literature (18, 19). In all cases, the full-width-at-half-maxima (FWHM) of the Rh $3d_{5/2}$ peaks for the rhodium oxide standards were less than 1.7 eV.

Deconvolution of XPS spectra was performed by using a Gaussian lineshape and constraining the contributions to the Rh(3*d*) peaks from the spin–orbital splitting (Rh $3d_{5/2,\,3/2}$) to a ratio of 0.67. In some instances, the fitting of the measured peaks by a single Rh($3d_{5/2,\,3/2}$) doublet did not result in a reasonable FWHM (below 3 eV) and goodness-of-fit. In these cases, two Rh($3d_{5/2,\,3/2}$) doublets were used, either rhodium metal and rhodium oxide or two different rhodium oxides. After assigning one doublet to an appropriate binding energy of rhodium metal or oxide, a second doublet was added at a binding energy such that the sum of the two doublet peaks matched the acquired peak. This fitting routine further optimized the peak positions, intensities, and FWHM's of the lines to achieve an optimum goodness-of-fit between experimental and summed curves.

TABLE 1

X-Ray Photoelectron Spectroscopy of Rh($3d_{5/2}$) Binding Energies of Rhodium Oxide Standards

Composition	Structure	Rh($3d_{5/2}$) binding energy (eV)	FWHM Rh($3d_{5/2}$) (eV)	Reference
Rhodium metal	fcc	307.0–307.3	—	17, 18
Rh_2O_3	Hexagonal	308.1–308.6	—	17–19, 22
Rh_2O_3	Hexagonal	308.1	1.4	This work
Rh_2O_3	Orthorhombic (HT, LP)	308.4	1.4	This work
RhO_2	Tetragonal	309.4	1.7	This work
RhOOH	Tetragonal	308.0–308.6	—	18, 19
RhOOH or RhO_2	Unknown	309.3	—	33

RESULTS AND DISCUSSION

Effects of Aging on Rhodium

Both HRTEM images and XPS reveal that the rhodium catalyst undergoes oxidation and coarsening upon aging in air. The following discussion describes the characteristics of the rhodium catalyst as a function of time and temperature.

As shown in Fig. 1, the unaged catalyst consists of small rhodium particles averaging approximately 10 Å in diameter and appearing to be near-spherical in shape.

After aging for 9 h at 500°C, HRTEM images reveal the presence of both metal and oxide particles. While the rhodium metal particles are only slightly larger (12 Å) than those of the fresh catalysts (10 Å), the rhodium oxide particles are substantially larger. A typical oxide particle is shown in Fig. 2a. It has a diameter of approximately 35 Å and exhibits a disordered structure. A diffractogram of the particle (Fig. 2b) reveals the (121) and $(10\overline{3})$ planes originating from the high-temperature, high-pressure orthorhombic Rh_2O_3 phase. The distances between the (121) and $(10\overline{3})$ planes are 2.27 and 2.19 Å, respectively, and the angle between the planes is 95.8°, which is close to the calculated value of 95.6°.

Upon further aging (56 h at 500°C), there is an apparent change in the rhodium oxide particle morphology. The hemispherical rhodium oxide structures formed after aging for 9 h transform into highly dispersed raft-like structures 15 to 60 Å in diameter. Viewed edge-on (see Fig. 2c) these

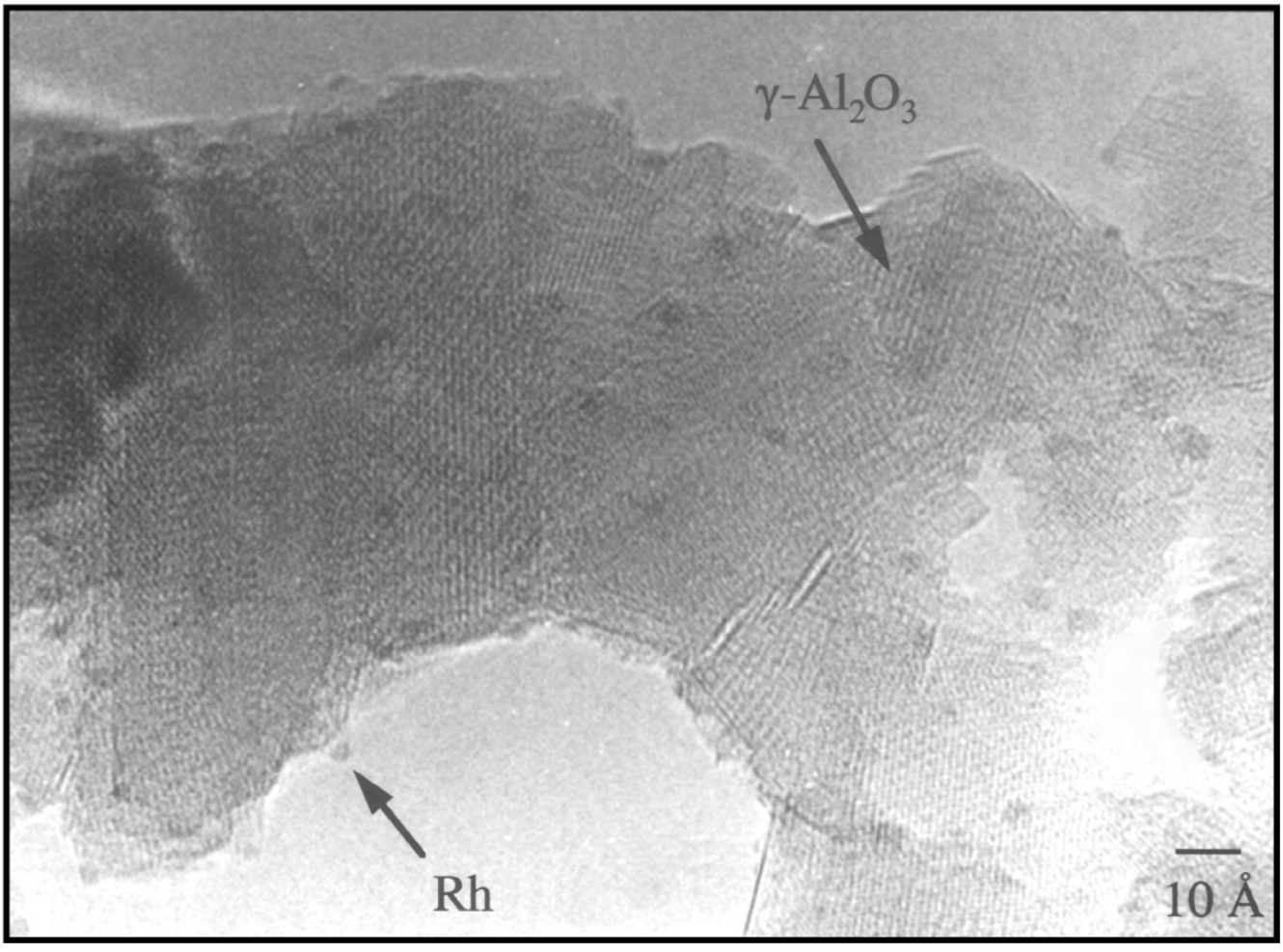

FIG. 1. High-resolution transmission electron (HRTEM) image of an as-prepared catalyst revealing well-dispersed, small rhodium particles, averaging approximately 10 Å in diameter.

raft-like structures are observed to be between one and two monolayers thick. Imaging of these structures in plan-view by HRTEM is difficult because of the small thickness of the oxide relative to that due to the alumina support. As a consequence, it is impossible to assign these raft-like features to a particular phase of rhodium oxide. It is quite conceivable, though, that the structures represent an epitaxial layer of rhodium oxide on the surface of either γ-alumina or one of the transitional phases.

After aging for 102 h at 500°C, the oxide structures coarsen and thicken to the point where imaging of these structures is possible in plan-view. Figure 3 (top) shows a thicker, less dispersed rhodium oxide particle of approximately 180 Å in diameter. Here, the lattice fringe spacings of 5.1 and 4.4 Å are unusually large. This fringe spacing is larger than any of the known interplanar spacings of the hexagonal Rh_2O_3, HT, HP orthorhombic Rh_2O_3, HT, LP orthorhombic Rh_2O_3, orthorhombic RhOOH, and hexagonal $HRhO_2$ structures. There are many possible explanations for these unusually large fringe spacings observed in Fig. 3 (top). One interpretation is that the dispersed rhodium oxide exhibits an epitaxial relationship with the support, which slightly alters the structure of the dispersed oxide. By using the alumina support as a template, a thin, metastable rhodium oxide phase with some resemblance of its bulk may be formed. In this case, the fringes in Fig. 3 (top) can be identified as the 1/2 $(10\bar{1})$ and 1/2 (111) planes of RhO_2. The diffractogram (Fig. 3 (bottom)) indicates that the angle between the planes is 107.9°, which is close to the calculated value of 108.1°. Note that the particle shown in Fig. 3 (top) exhibits a slightly disordered structure. The alternative possibility that the large fringe spacings are due to the formation of a rhodium aluminate structure may be excluded for two reasons. First, both the normal and inverse spinel-based transition metal aluminate structures require a 2+ valence state for the transition metal ion, in which case the Rh($3d_{5/2}$) XPS signal should reveal a Rh^{2+} state occurring at a binding energy between that of the Rh^0

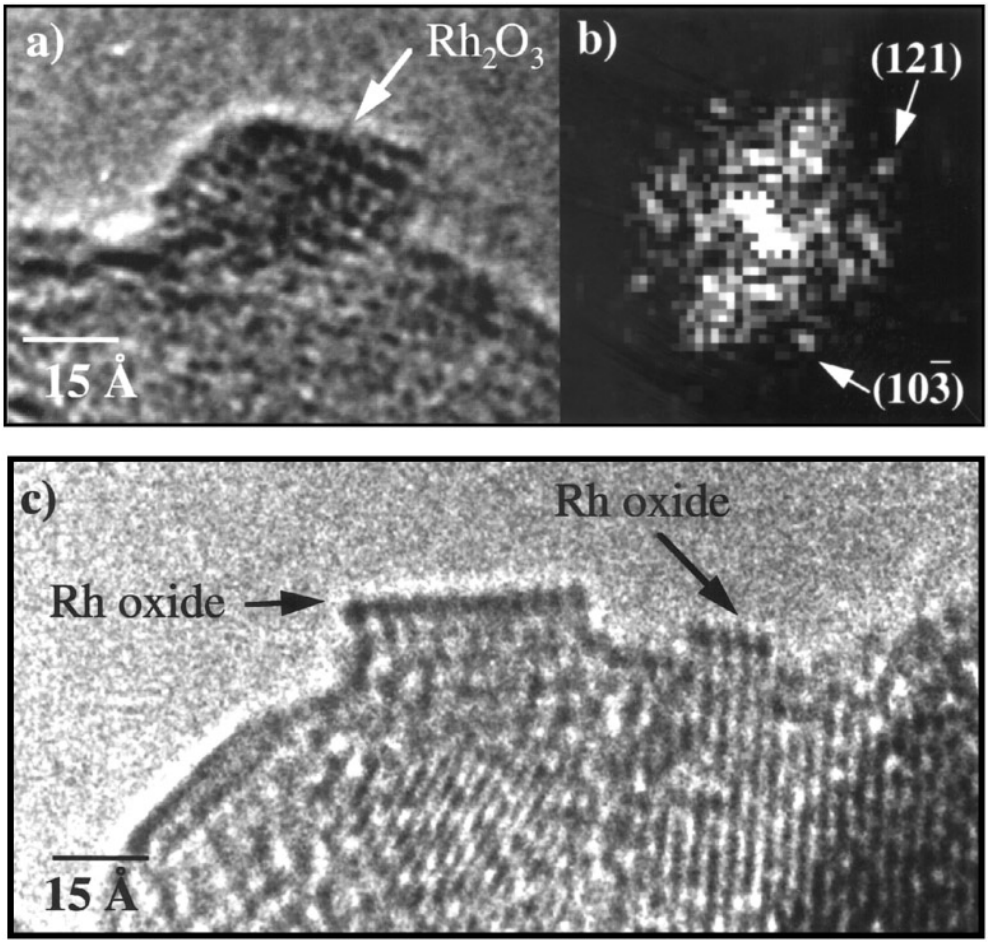

FIG. 2. (a) HRTEM image of rhodium oxide particle formed after aging 9 h at 500°C; (b) diffractogram of (a) revealing reflections corresponding to the high-temperature, high-pressure orthorhombic Rh_2O_3 phase; and (c) HRTEM image of a dispersed rhodium oxide structure, viewed edge-on, formed after aging 56 h at 500°C.

and Rh^{3+} states. An attempt to observe Rh^{2+} was made, by means of electron paramagnetic resonance (EPR), but no evidence was found for this cation. Second, the observed fringe spacings exceed the Rh–Rh spacings expected for a spinel structure, based on the lattice parameters of transition metal aluminates (20) (viz., 8.08 Å for $MgAl_2O_4$ and $ZnAl_2O_4$ and 8.26 Å for $MnAl_2O_4$).

Aging at 850°C results in the rapid oxidation of rhodium and the continued increase in the size of the rhodium oxide particles as aging progresses. The presence of fairly dispersed oxide structures (Fig. 4a) is observed after aging for 4 h. These particles are between 20 and 30 Å in diameter, between 2 and 4 monolayers in height, and appear to wet the alumina support to a lesser degree than the highly dispersed rhodium oxide structures formed after aging for 56 h at 500°C. Further aging (25 h) results in severe coarsening of the rhodium oxide particles and the formation of the HT, HP orthorhombic Rh_2O_3 structure. An example of such a structure is presented in Fig. 4b which illustrates a particle with a diameter of 72 Å. The diffractogram (Fig. 4c) of the particle reveals the $(1\bar{1}1)$ and $(11\bar{1})$ planes. The angle between these planes is 100.2°, which is close to the calculated angle of 100.7°. The accompanying selected-area electron diffraction pattern (Fig. 4f) reveals reflections corresponding to the HT, HP orthorhombic Rh_2O_3 (circled) and θ-alumina structures. Aging for 56 h results in the additional coarsening of the rhodium oxide particles. Figure 4d shows a rhodium oxide particle with a diameter of 150 Å. The diffractogram of the particle (Fig. 4e) reveals the (112) and $(02\bar{1})$ planes, corresponding to spacings of 2.6 and 2.5 Å, respectively, characteristic of the HT, HP orthorhombic Rh_2O_3 structure. These planes are separated by an angle of 77.4°, which is close to the calculated angle of 77.8°.

Aging for 5 h at 1000°C results in extensive coarsening of the rhodium oxide particles, as well as the support. The low magnification image presented in Fig. 5 shows five rhodium oxide particles (labeled 1–5) with diameters ranging between 31 and 61 nm. These rhodium oxide particles occur

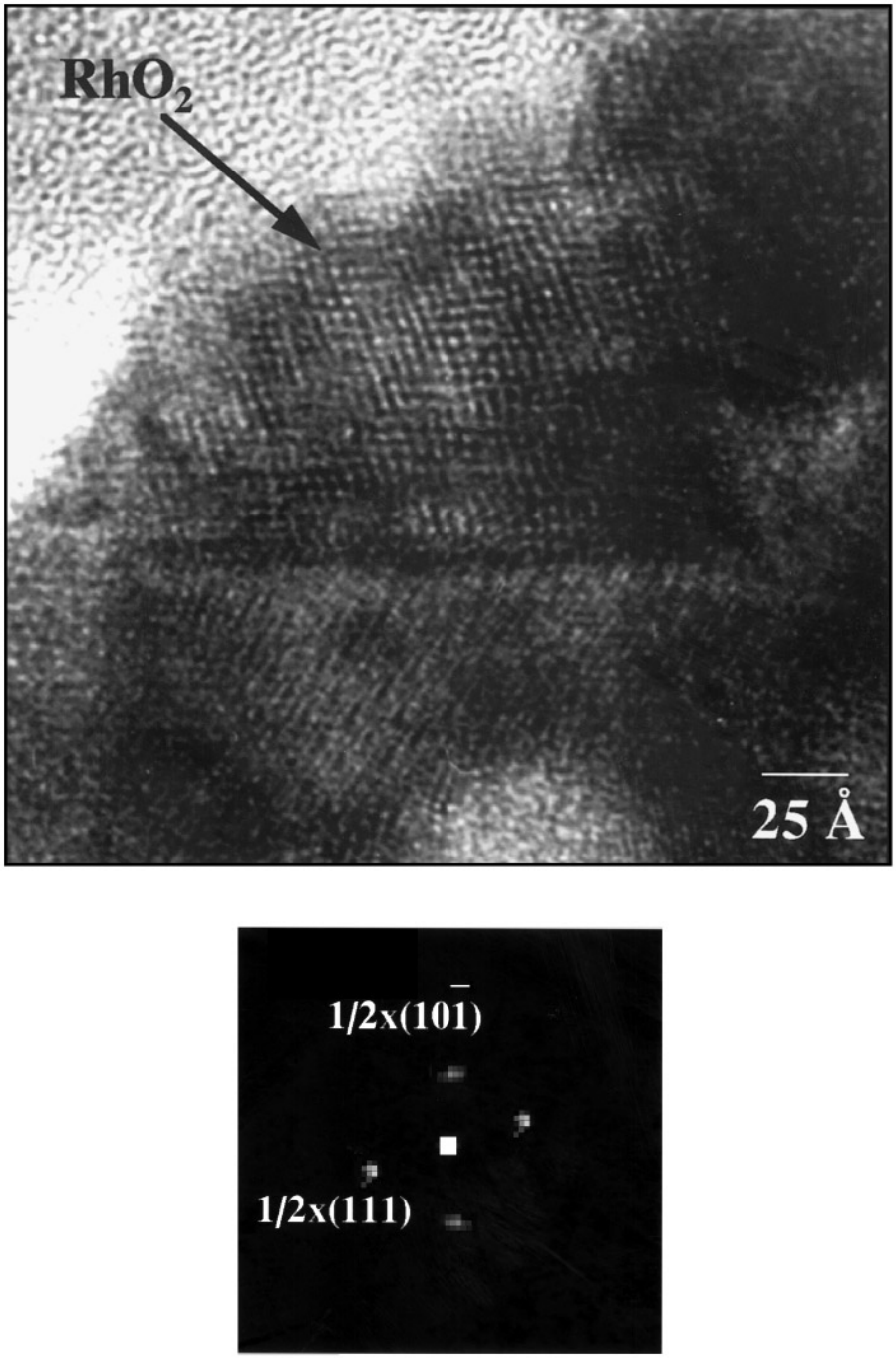

FIG. 3. (Top) HRTEM image of rhodium oxide formed after aging 102 h at 500°C, (bottom) diffractogram of (top) revealing reflections corresponding to the RhO_2 structure.

in the presence of the α-alumina and are larger than the grains of δ- and θ-alumina. Further analysis indicates the coexistence of both the HT, HP orthorhombic Rh_2O_3 and the RhO_2 phases. Particle A which has a diameter of 56 nm is shown at a higher magnification in Fig. 6a. A diffractogram of the particle, presented in Fig. 6b, reveals the (210) and (1$\bar{1}$3) reflections occurring from the HT, HP orthorhombic Rh_2O_3 phase. The angle measured between the (210) and (1$\bar{1}$3) reflections is 80.6°, compared to the calculated value of 79.3°. Figure 7a shows an RhO_2 particle of 19 nm in diameter, viewed along its (110) direction. The diffractogram (Fig. 7b) reveals reflections corresponding to the (111) RhO_2 planes that are separated by 2.2 Å. The angle measured between the planes is 92.6°, which is close to

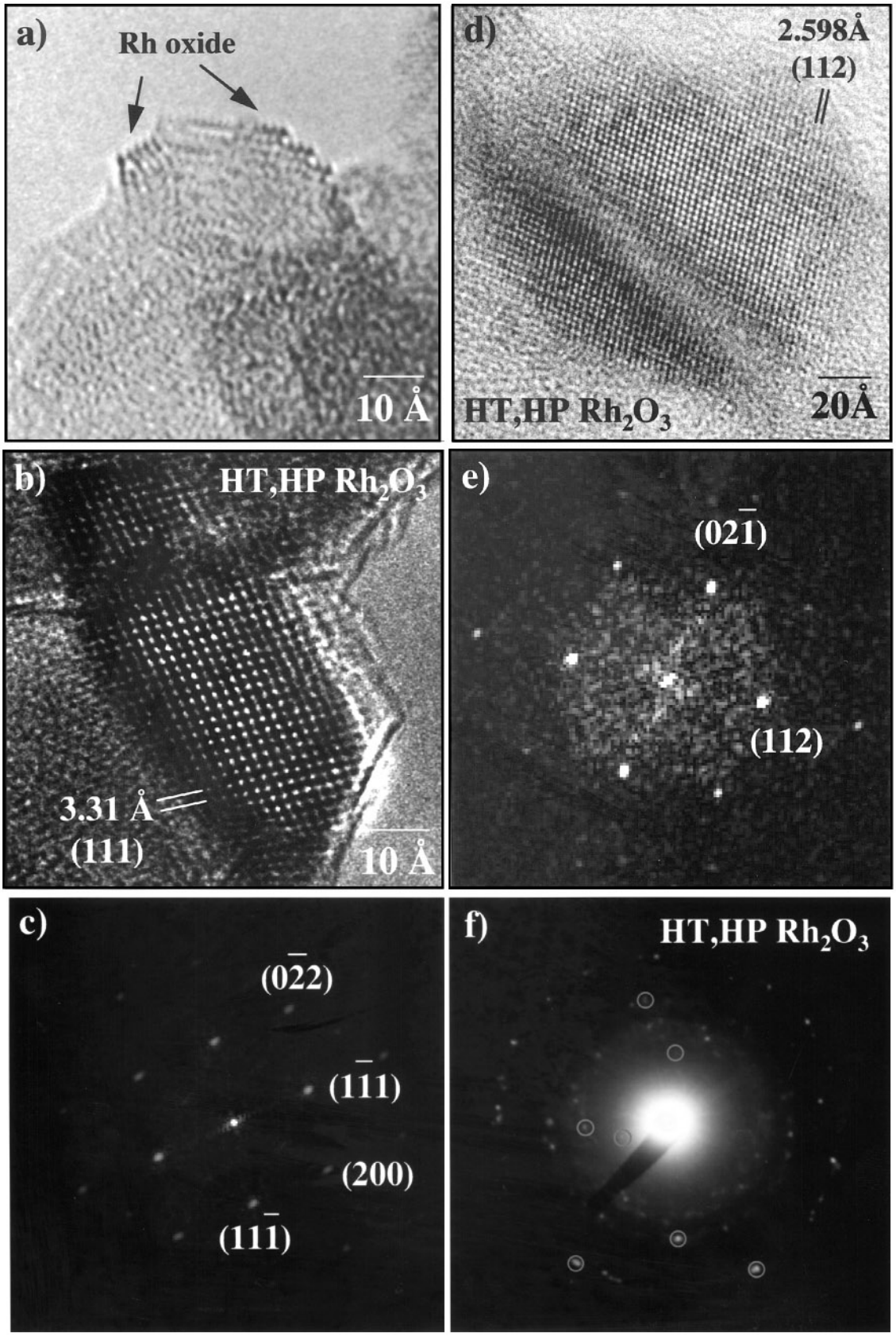

FIG. 4. (a) HRTEM image of a partially dispersed rhodium oxide structure formed after aging 4 h at 850°C; (b) HRTEM image of a large rhodium oxide particle formed after aging 25 h at 850°C; (c) diffractogram of (b) revealing reflections corresponding to the high-temperature, high-pressure orthorhombic Rh_2O_3 phase; (d) HRTEM image of rhodium oxide particle formed after 56 h at 850°C; (e) diffractogram of (d) revealing reflections corresponding to high-temperature, high-pressure orthorhombic Rh_2O_3 phase; and (f) electron diffraction pattern of Rh/alumina after aging 25 h at 850°C showing reflections originating from the high-temperature, high-pressure orthorhombic Rh_2O_3 phase.

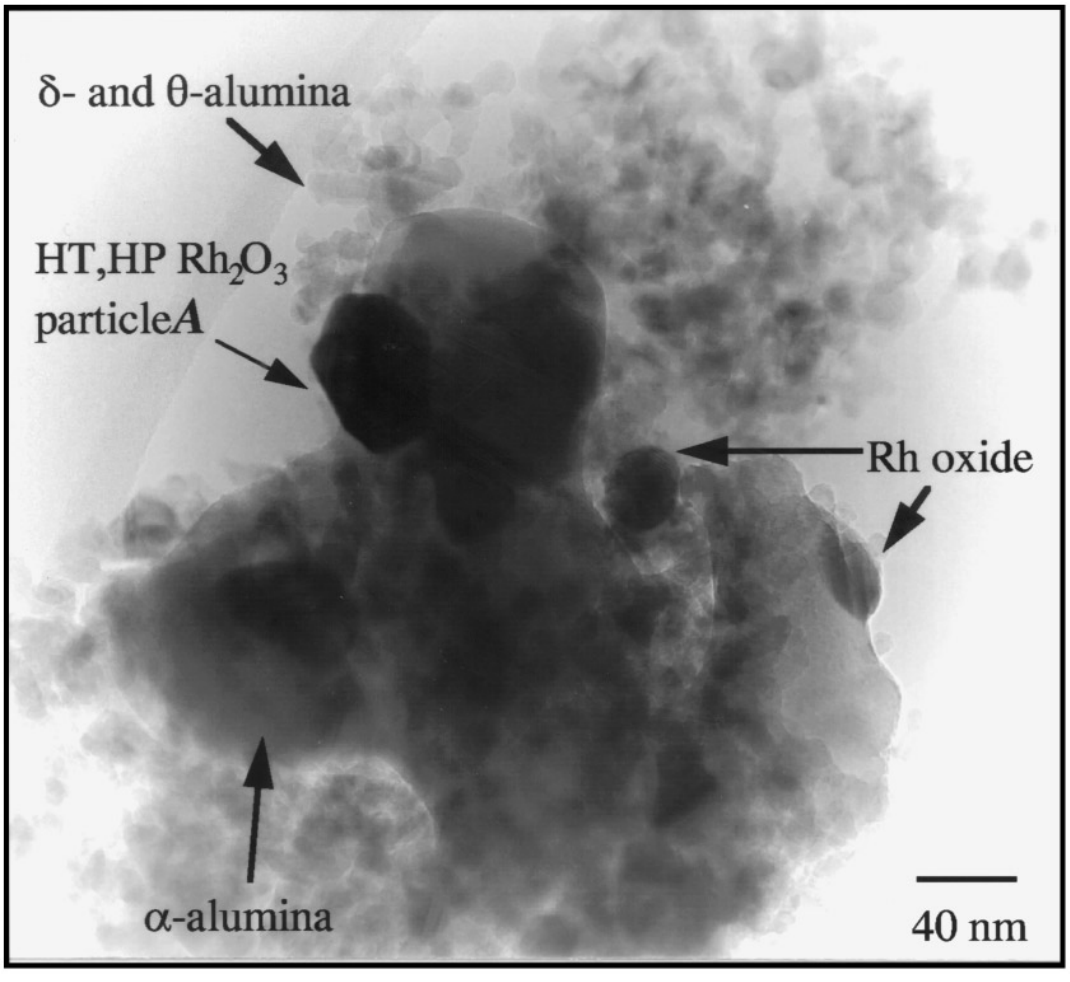

FIG. 5. Low magnification TEM image showing the formation of α-alumina and large rhodium oxide particles after aging 5 h at 1000°C.

the calculated value of 91.5°. The particle is almost spherical in shape, with two developing surface facets, as marked by "f." The strong contrast change observed in the interior of the particle is indicative of twinning.

XPS measurements also reveal that the supported rhodium particles undergo oxidation during aging in air. Figure 8 displays XPS spectra of the Rh($3d_{5/2,\,3/2}$) region taken after aging of alumina-supported Rh for different times at different temperatures. Also shown are the component peaks determined by deconvolution. The binding energies, full-width-at-half-maxima (FWHM), and percentage of total signal intensity for each component peak are given in Table 2. Each of the XPS spectra presented in Fig. 8 can be deconvoluted into two peaks, the positions of which

TABLE 2

Quantification of XPS Rh($3d_{5/2}$) Signal Obtained from Aged Samples

Time (h)	Temp. (°C)	Rh BE (eV)	% total	FWHM	Rh_2O_3 BE (eV)	% total	FWHM	RhO_2 BE (eV)	% total	FWHM	Goodness-of-fit
9	500	307.3	55	2.5	—	—	—	309.3	45	2.7	0.10
56	500	307.8	43	2.8	—	—	—	309.5	57	2.7	0.14
102	500	—	—	—	308.5	14	1.9	309.3	86	2.3	0.35
4	850	307.5	33	2.6	—	—	—	309.3	67	2.5	0.03
25	850	—	—	—	308.6	18	1.8	309.8	82	2.1	0.17
56	850	—	—	—	308.5	16	1.3	309.3	84	2.1	0.30
5	1000	—	—	—	308.1	19	2.0	309.9	81	2.0	0.72

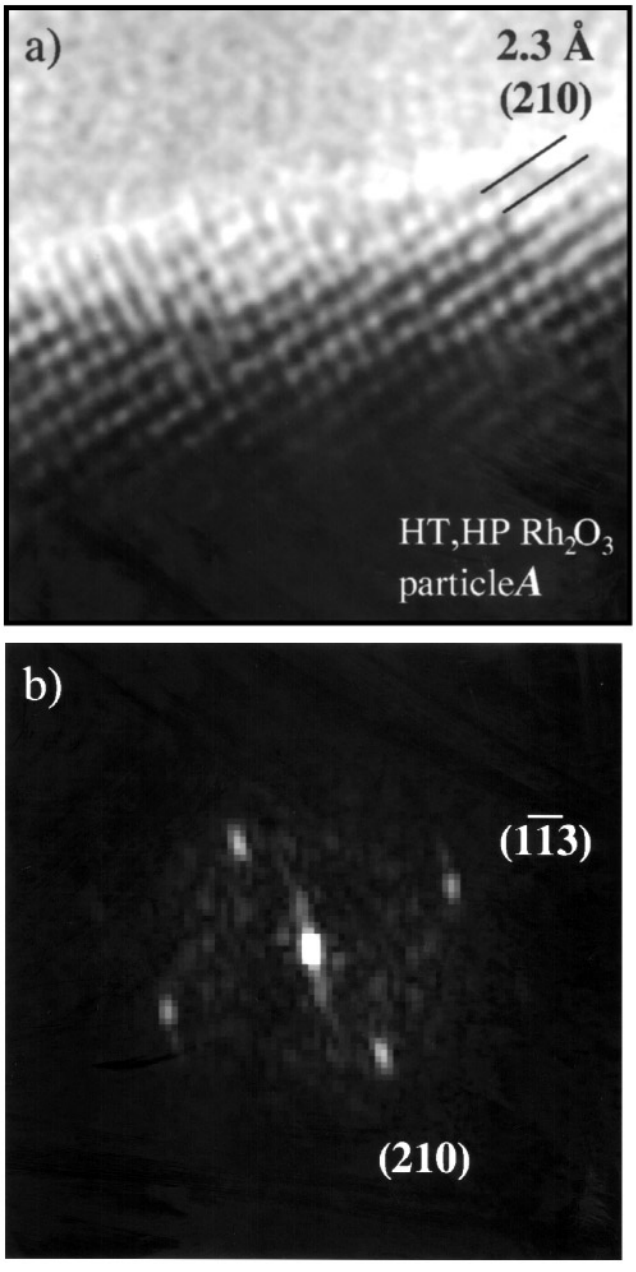

FIG. 6. (a) HRTEM image of particle A from Fig. 5 formed after aging 5 h at 1000°C and (b) diffractogram of (a) reveals reflections corresponding to the high-temperature, high-pressure orthorhombic Rh_2O_3 phase.

depend on the temperature and duration of aging. The binding energies for the component peaks occur at 307.3–307.8, 308.1–308.5, and 309.3–309.9 eV. Based on the measured binding energies of rhodium metal and different forms of rhodium oxide, XPS peaks in the range 307.3–307.8, 308.1–308.5, and 309.3–309.9 eV are assigned to Rh^0, Rh_2O_3 (i.e., Rh^{3+}), and RhO_2 (i.e., Rh^{4+}). As discussed below, the third of these assignments needs to be considered carefully, since the presence of large amounts of RhO_2 suggested by the XPS results presented in Table 2 is inconsistent with the observed HRTEM images.

Table 2 shows that as the temperature and time of aging increase, the proportion of Rh metal present decreases, and the proportions of Rh_2O_3 and RhO_2 increase. These data suggest that in excess of 40% of the Rh is present as RhO_2 after aging Rh/γ-Al_2O_3 for 102 h at 500°C, 25 or 56 h at 850°C, or 5 h at 1000°C. As noted above, interpretation of the HRTEM images shown in Fig. 3 suggests that after aging for 102 h at 500°C, the observed oxide particles are best ascribed to RhO_2 grown epitaxially on alumina. In contrast, analysis of HRTEM images taken after aging for either 25 or 56 h at 850°C show no evidence of RhO_2, and all of the oxide is identified as HT, HP orthorhombic Rh_2O_3. On the other hand, a combination of large particles of HT, HP orthorhombic Rh_2O_3 and smaller particles of RhO_2 are seen after aging for 5 h at 1000°C (see Fig. 7). These observations suggest that the XPS peak at 309 eV may be due to Rh^{4+} present in RhO_2 as well as "super-stoichiometric" Rh_2O_3 (12, 13, 33, 34). Thus, it is conceivable that the outermost layers of Rh_2O_3 have an O/Rh ratio in excess of 1.5. An alternative interpretation for the peak at 309 eV is that it is due to very small particles (<20 Å) of Rh_2O_3. In such case, the shift in binding energies from 308 to 309 eV would be ascribed to screening effects. Such an interpretation or some other would need to be invoked to explain the presence of an XPS peak at 309 eV following aging at 850°C, since the HRTEM images show no evidence of RhO_2.

The FWHM of the Rh^0 and Rh^{4+} components are larger than those observed for bulk phases (~1.5–1.7). This might be due to a combination of final and/or initial state effects, which in the case of metals are known to increase the FWHM up to 3 eV (21). The FWHM of the peak at 309 eV decreases monotonically from 2.7 to 2.0 eV as the aging temperature and time increase. This trend is consistent with the HRTEM observation, which shows an increase in particle size as the severity of oxidation condition increases.

While HRTEM and XPS both show evidence for the formation of RhO_2 and Rh_2O_3 upon high-temperature oxidation of Rh/γ-Al_2O_3, there remains the question of whether the oxide phases observed at a given temperature are those expected on the basis of thermodynamic equilibrium. The most comprehensive pressure–temperature phase diagram is that reported by Muller and Roy (22). As shown in Fig. 9, tetragonal RhO_2 is stable at low temperature and high O_2 pressure. At $P_{O_2} = 0.2$ atm, hexagonal Rh_2O_3 becomes the stable phase above 680°C and HT, LP orthorhombic Rh_2O_3 becomes the stable phase above 900°C. More recent studies by Carol and Mann (23) indicate that the phase boundary separating the hexagonal and HT, LP orthorhombic polymorphs of Rh_2O_3 is not as sharp as that suggested by Muller and Roy, and that in fact both polymorphs can coexist between temperatures 700 and 800°C. Figure 9 shows that for $P_{O_2} = 0.2$ atm, HT, LP orthorhombic Rh_2O_3 is unstable

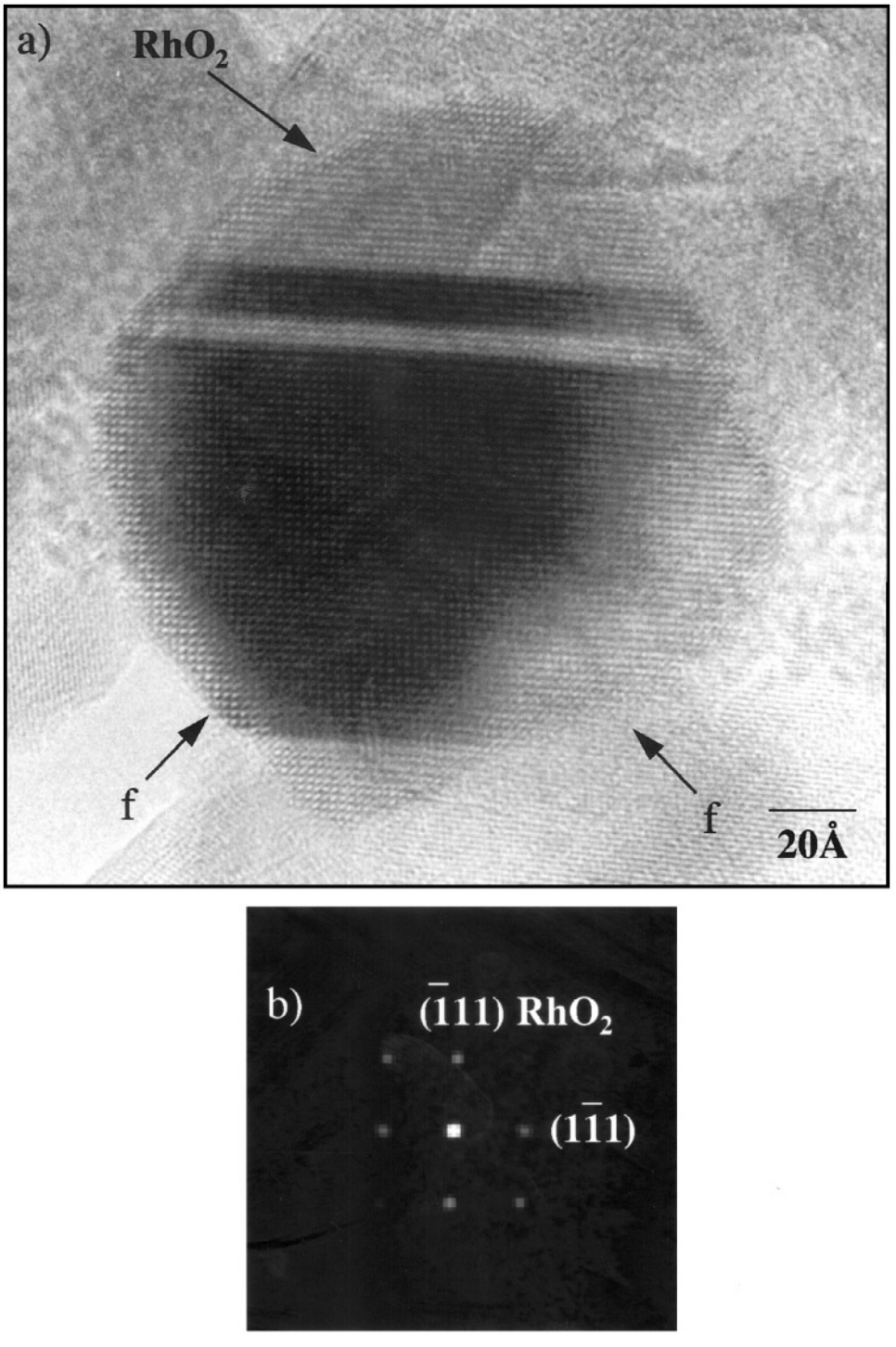

FIG. 7. (a) HRTEM image of an internally twinned rhodium oxide particle with emerging surface facets labeled "f" and (b) diffractogram of (a) reveals reflections corresponding to the RhO_2 phase.

relative to metallic Rh above 1020°C. Based on this phase diagram, we would expect RhO_2 to be the thermodynamically favorable phase at 500°C, and HT, LP orthorhombic Rh_2O_3 to be the stable phase at 850 and 1000°C. The presence of HT, HP orthorhombic Rh_2O_3 at 500, 850, and 1000°C and of RhO_2 at 1000°C suggests that the distribution of rhodium oxide phases formed during high-temperature aging of alumina-supported rhodium may be governed by kinetics rather than thermodynamics and may also be influenced by the epitaxy of the rhodium oxide particles with the

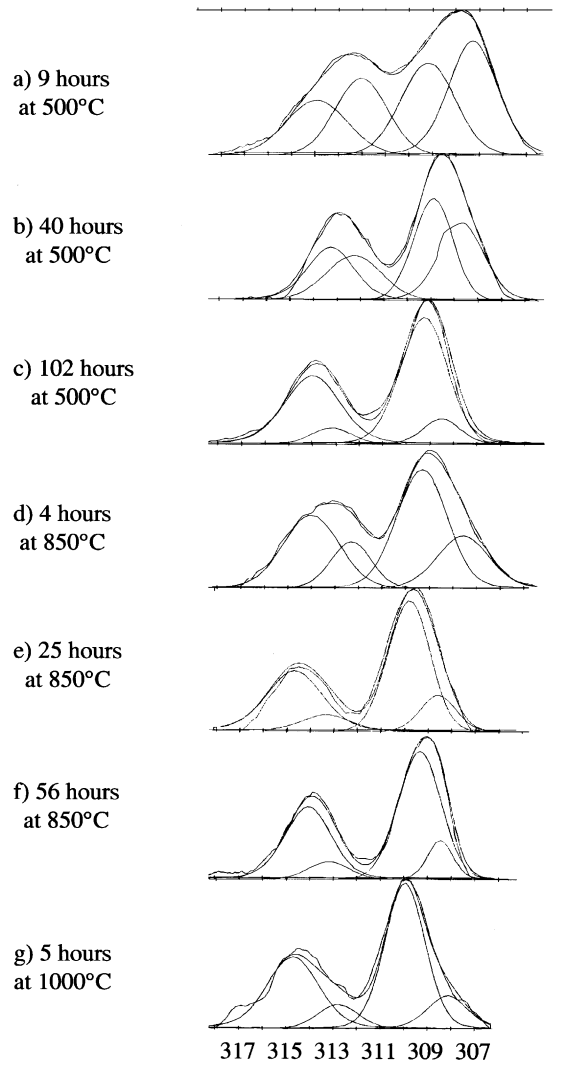

FIG. 8. X-ray photoelectron spectra (XPS) of the Rh($3d_{5/2}$, $3d_{3/2}$) peaks: (a) 9 h at 500°C, (b) 56 h at 500°C, (c) 102 h at 500°C, (d) 4 h at 850°C, (e) 25 h at 850°C, (f) 56 h at 850°C, and (g) 5 h at 1000°C.

alumina surface. In a recent study performed in our laboratory, we found that the epitaxy of rhodium oxide particles on α-alumina support stabilized the formation of hexagonal Rh_2O_3 at temperatures of 500 and 850°C (24). The presence of RhO_2 at 1000°C is harder to rationalize. It is conceivable that during the increase in furnace temperature, some particles of RhO_2 are formed before the sample reaches 1000°C and that these particles are only partially transformed to orthorhombic Rh_2O_3 during the 5 h at 1000°C. This problem was probably avoided at 850°C since the shortest aging period at that temperature was 25 h.

Effects of Aging on Alumina

The X-ray diffraction pattern shown in Fig. 10a indicates that the pure, unaged support is a mixture of both the γ- and δ-alumina phases, but peak overlap makes quantification of the relative amounts difficult. Aging in air at 1000°C for 5 h results in the formation of both δ- and θ-alumina (Fig. 10b). In the presence of Rh, the transformation of the support is accelerated. Figure 10c shows that upon aging at 1000°C, the alumina catalyst support begins to transform to α-alumina within 5 h. The sharpness of the α-alumina peaks present in Fig. 10c reflects the significant grain growth that occurs upon the formation of α-alumina grains. Comparison of the diffraction patterns in Figs. 10b and 10c demonstrates that rhodium accelerates the transformation of γ- to α-alumina.

Additional evidence for the grain growth of the alumina support upon formation of α-alumina is observed in TEM images. Figure 11 shows the typical alumina grain structure formed upon aging the supported catalyst for 5 h at 1000°C. The formation of the α-alumina phase results in a dramatic densification and grain growth of the support. Selected-area electron diffraction (not shown) indicates that the smaller grains are δ- and θ-alumina while the large grains are α-alumina. The size of the α-alumina grains appears to be several orders of magnitude larger than that of the δ- and θ-alumina grains, indicating a sharp decrease in the surface area of the support.

The results presented in Figs. 10 and 11 clearly demonstrate that the alumina support undergoes significant changes upon aging via the processes of grain growth, densification, and phase transformation. Of these processes, the most significant change is the dramatic loss of support surface area following the formation of α-alumina. Typically, for pure alumina, the phase transformation of γ-alumina occurs through the formation of δ-alumina at approximately 700°C, θ-alumina at approximately 1000°C, and finally α-alumina at approximately 1200°C (25). As

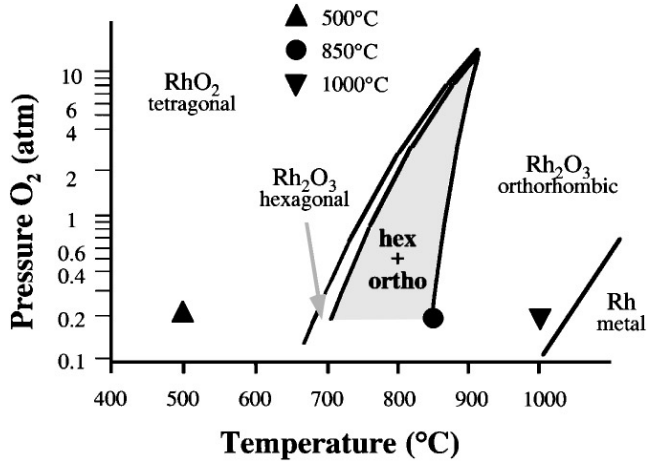

FIG. 9. Bulk rhodium oxide phase stability as a function of pressure versus temperature, adapted from Muller and Roy (22) and Carol and Mann (23).

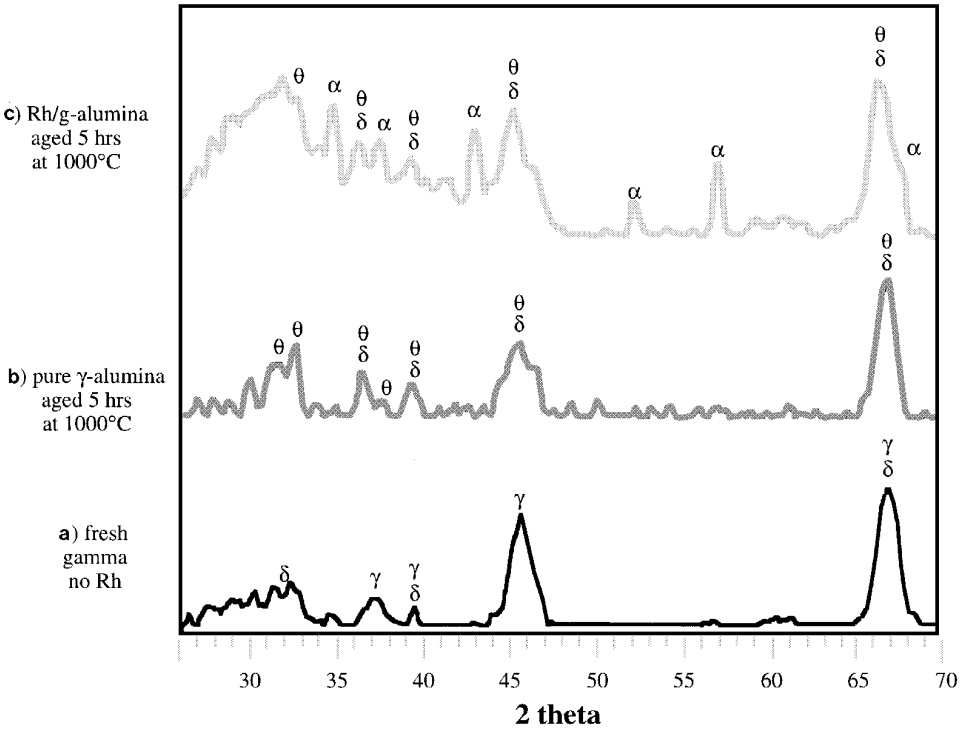

FIG. 10. X-ray diffraction patterns of pure alumina support: (a) as-received support consists of γ- and δ-alumina, (b) pure support aged for 5 h at 1000°C transforms to δ- and θ-alumina, and (c) Rh/γ-alumina catalysts aged for 5 h at 1000°C support transforms to δ-, θ-, and α-alumina.

reported in the literature (25–34), there may be a combination of factors controlling the transformation of γ-alumina to α-alumina, including the creation, diffusion, ordering, and annihilation of point defects and stress formation. In the γ-alumina phase, the structure is a disordered spinel with a random distribution of aluminum vacancies and a mixed occupation of both octahedral and tetrahedral sites by Al (25). During the γ- to δ-phase transformation, oxygen and aluminum vacancies undergo self annihilation such that the tetrahedrally coordinated Al^{3+} cations are converted to octahedrally coordinated Al^{3+} cations (26). Accompanying this process is a diffusional ordering of the Al tetrahedral vacancies causing the unit cell of the δ-phase to increase by 2-fold along its x axis and by 1.5-fold along its y axis (26). The δ- to θ-alumina transformation is also believed to be a diffusive process, but the details of the structural rearrangement on the atomic level are not well understood (27, 28). It has been proposed that the θ- to α-alumina transformation occurs via either a "synchoshear" (martensitic) process, requiring a critical grain size of the θ-alumina prior to transformation (27), or a nucleation and growth type process (28).

Comparison of the X-ray diffraction patterns presented in Figs. 10a and 10c demonstrates that the phase transformation of the support is accelerated by the presence of rhodium. The rhodium appears to reduce the time and temperature necessary for the phase transformations of the alumina, as demonstrated by the formation of θ-alumina after aging pure alumina for 5 h at 1000°C and of α-alumina after aging Rh/alumina for the same time and temperature. A similar lowering in the transformation temperature has been reported by McCabe *et al.* (15), who observed the formation of α-alumina after aging 0.4 wt% rhodium supported on the same alumina for 4 h at 1050°C.

Previous studies have shown that the transformation of γ- to α-alumina can be either accelerated or retarded by the presence of small amounts of oxide impurities (29–34). Oxides such as Fe_2O_3, TiO_2, MgO, NiO, CuO, MnO_2, V_2O_5, and PtO have been found to encourage the transformation to α-alumina at temperatures as low as 900°C (29–33). Likewise, rhodium oxide and platinum oxide have been reported to accelerate the formation of α-alumina at 1050°C (15) and 950°C (32), respectively. In contrast, oxides of some of the rare-earths such as La and Ce are known to have an inhibiting effect, increasing the transformation temperature up to 1300°C (34). How metal oxide impurities accelerate or inhibit the phase transformation processes is the subject of ongoing research (26–28).

One of the most successful attempts to explain the effects of cation impurities on the phase transformation of alumina is that due to Burtin *et al.* (33). The transformation is ascribed to dehydroxylation of γ-alumina by the removal of water followed by the formation of α-alumina as a consequence of the annihilation of anion and cation vacancies,

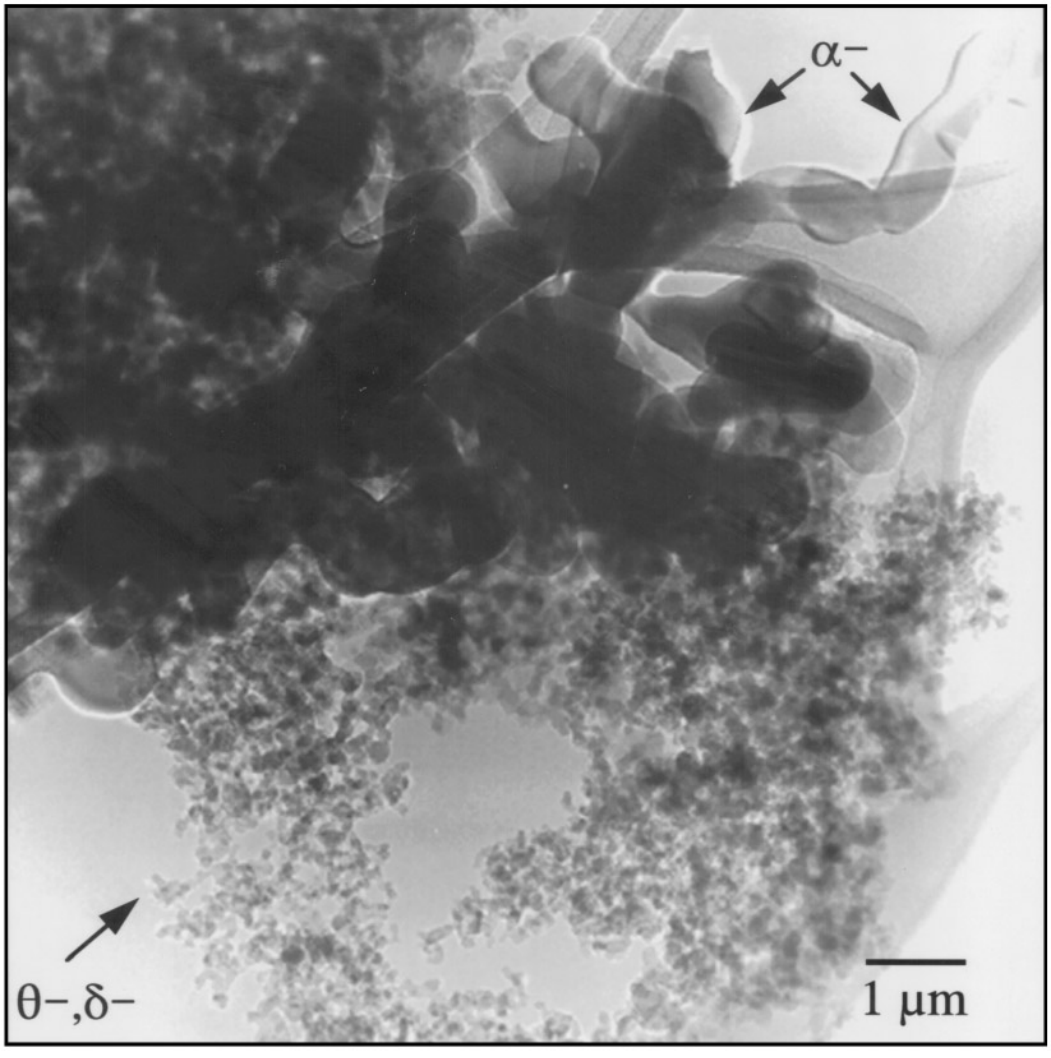

FIG. 11. Low magnification TEM image of large α-alumina grains and smaller δ- and θ-alumina formed after aging Rh/γ-alumina 5 h at 1000°C.

with the latter process taken to be rate limiting. Impurity cations introduced into γ-alumina are assumed to alter the concentrations of vacancies, which in turn alter the rate of the γ- to α-alumina transformation. The extent to which a given cation accelerates or inhibits the rate of α-alumina formation depends on its valence and a parameter which is a function of its radius.

Based on the work of Burtin *et al.* (33), it is possible to differentiate between inhibitor and accelerator cations by their location on a plane defined by cation valence and radius. Figure 12 shows that with some exceptions, inhibitor cations (hollow circles) have a high valence and large radius, whereas accelerator cations (filled triangles) have a low valence and small radius. Rh^{3+} clearly lies in the portion of the plane occupied by the accelerator cations. Rh^{4+} would also be expected to act as an accelerator since while its valence is higher than that of Rh^{3+}, its radius is smaller.

CONCLUSIONS

Aging of a Rh/γ-alumina catalyst in air causes a variety of microstructural changes in both the rhodium and alumina phases. The presence of rhodium on the support accelerates the transformation of the support from γ- to α-alumina. This effect is attributed to an increase in the number of defects in the alumina support due to the incorporation of a small number of rhodium cations. The rhodium initially present as 10 Å metal particles undergoes oxidation and sintering during thermal aging. At 500°C, highly dispersed raft-like structures are formed. Prolonged aging at this temperature leads to the appearance of small particles of orthorhombic Rh_2O_3. Aging at 850 and 1000°C produces progressively larger particles of HT, HP orthorhombic Rh_2O_3. Large particles of RhO_2 are also observed after aging at 1000°C. The distribution of rhodium phases present at different temperatures is not fully consistent with that

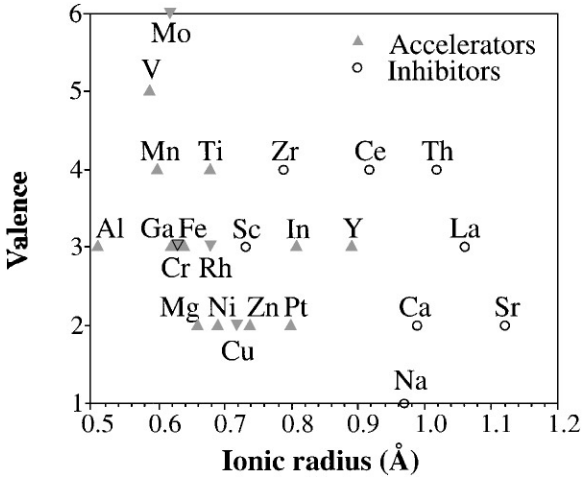

FIG. 12. Map of impurity cation radius versus valence state. Accelerators (filled triangles) of γ- to α-alumina phase transformation typically exhibit small radius and valence. Inhibitors (hollow circles) typically exhibit large radius and valence.

expected for thermodynamic equilibrium, suggesting that both the epitaxy of the rhodium oxide on the support and the kinetics of rhodium oxide formation play an important role in defining which phases are formed.

ACKNOWLEDGMENTS

This work was supported by the Office of Chemical Sciences, Division of Basic Energy Sciences, of the U.S. Department of Energy under Contract DE-AC03-76SF00098 at the Lawrence Berkeley National Laboratory. Access to the facilities at the National Center for Electron Microscopy is acknowledged. Z. Weng-Sieh recognizes support through a Noyce Foundation Fellowship.

REFERENCES

1. Bosch, H., and Jaansen, F., *Catal. Today* **2**, 369 (1988).
2. Taylor, K. C., *Catal. Rev. Sci. Technol.* **35**, 457 (1993).
3. "Clean Air Act Amendments, Detailed Summary of Titles," U.S. EPA, Nov. 30, 1990.
4. Yao, H. C., Japar, S., and Shelef, M., *J. Catal.* **50**, 407 (1977).
5. Yao, H. C., Gandhi, H. S., and Shelef, M., *in* "Metal-Support and Metal-Additive Effects in Catalysis" (B. Imelik *et al.*, Eds.).
6. Vis, J. C., van'T Blik, H. F. J., Huizinga, T., van Grondelle, J., and Prins, R., *J. Catal.* **95**, 333 (1985).
7. Beck, D. D., and Carr, C. J., *J. Catal.* **144**, 296 (1993); ibid., **144**, 311 (1993).
8. Burkhardt, J., and Schmidt, L. D., *J. Catal.* **116**, 240 (1989).
9. Yates, D. J. C., and Prestidge, E. B., *J. Catal.* **106**, 549 (1987).
10. Usmen, R. K., McCabe, R. W., Haack, L. P., Graham, G. W., Hepburn, J., and Watkins, W. L. H., *J. Catal.* **134**, 702 (1992).
11. Duprez, D., Delahay, G., Abdererrahim, H., and Grimblot, J., *J. Chim. Phys.* **83**, 465 (1987).
12. Logan, A. D., Datye, A. K., and Houston, J. E., *Surf. Sci.* **245**, 280 (1991).
13. Logan, A. D., Braunschweig, E. J., Datye, A. K., and Smith, D. J., *Ultramicroscopy* **31**, 132 (1989).
14. Bayer, G., and Weidemann, H. G., *Thermochimica Acta* **15**, 213 (1976).
15. McCabe, R. W., Usmen, R. K., Ober, K., and Gandhi, H. S., *J. Catal.* **151**, 385 (1995).
16. Koyama, T., Bell, A. T., Weng-Sieh, Z., Gronsky, R., Engelke, F., King, T. S., and Pruski, M., *J. Catal.* **150**, 400 (1995).
17. Briggs, D., and Seah, M. P., "Practical Surface Analysis," Wiley, Chichester, 1990.
18. Barr, T. L., *J. Phys. Chem.* **82**, 1801 (1978).
19. Peuckert, M., *Surf. Sci.* **141**, 500 (1984).
20. Lide, D. R. (Ed.), "Handbook of Chem. and Phys.," CRC Press, Boca Raton, 1995.
21. Kuhrt, C., and Harsdorff, M., *Surf. Sci.* **245**, 173 (1991).
22. Muller, O., and Roy, R., *J. Less-Common Metals* **16**, 129 (1968).
23. Carol, L. A., and Mann, G. S., *Oxidation Metals* **34**, 1 (1990).
24. Weng-Sieh, Z., Gronsky, R., and Bell, A. T., submitted for publication.
25. Gitzen, W. H., "Alumina as a Ceramic Material," American Ceramics Society, Columbus, 1970.
26. Jarayam, V., and Levi, C. G., *Acta Metall.* **37**, 569 (1989).
27. Wynnyckyj, J. R., and Morris, C. G., *Met. Trans. B* **16**, 345 (1985).
28. Dynis, F. W., and Halloran, J. W., *J. Am. Ceram. Soc.* **65**, 442 (1982); Tucker, D. S., *J. Am. Ceram. Soc.* **68**, C163 (1985).
29. Wakao, Y., and Hibino, T., *Nagoya Kogyo Gijutsu Shinenko Hokoku* **11**, 588 (1962).
30. Bye, G. C., and Simpkin, G. T., *J. Am. Ceram. Soc.* **57**, 367 (1974).
31. Kurkova, N. S., Katsobashvili, Ya. R., and Akchurina, N. A., *Zhurnal Prikl.* **46**, 1002 (1973).
32. Kozlov, N. S., Lazarev, M. Ya., Mostovaya, L. Ya., and Stremok, I. P., *Kinetics Catal.* **14**, 1130 (1973).
33. Burtin, P., Brunelle, J. P., Pijolat, M., and Soustelle, M., *Appl. Catal.* **34**, 239 (1987); *Appl. Catal.* **34**, 225 (1987).
34. Wachowski, L., Kirszensztejn, P., Lopatlin, R., and Cazjkn, B., *Mater. Chem. Phys.* **37**, 29 (1994).
35. Wong, C., and McCabe, R. W., *J. Catal.* **107**, 535 (1987); *J. Catal.* **119**, 47 (1989).
36. Duprez, D., Delahay, G., Abdererrahim, H., and Grimblot, J., *J. Chim. Phys.* **83**, 465 (1987).
37. Tolia, A. A., Smiley, R. J., Delgass, W. N., Takoudis, C. G., and Weaver, M. J., *J. Catal.* **150**, 56 (1994).